Devonian Alaskan-type ultramafic–mafic intrusions and silicic igneous rocks along the southern Altai orogen: Implications on the Phanerozoic continental growth of the Altai orogen of the Central Asian Orogenic Belt

Xian-Tao Ye [a,b], Chuan-Lin Zhang [b,*], Hai-Bo Zou [c], Gang Zhou [d], Chun-Yan Yao [b], Yong-Guan Dong [b]

[a] Chinese Academy of Geological Sciences, Beijing 100037, PR China
[b] Nanjing Institute of Geology and Mineral Resources, Nanjing 210016, PR China
[c] Department of Geology and Geography, Auburn University, Auburn 36849-5305, USA
[d] Xinjiang Bureau of Geology and Mineral Resources, Urumuqi 830000, PR China

ARTICLE INFO

Article history:
Received 10 May 2014
Received in revised form 29 July 2014
Accepted 6 August 2014
Available online 13 August 2014

Keywords:
Ultramafic–mafic intrusions
Chinese Altai orogen
Underplating
Continental arc
Continental growth

ABSTRACT

In this contribution, we have carried out an integrated study of the petrography, geochronology, geochemistry and mineral chemistry for the Devonian Alaskan-type ultramafic–mafic complexes and granitoids widely distributed along the southern Altai orogen, in order to provide a better understanding of the continental growth process and the regional tectonic evolution. LA-ICPMS zircon U–Pb dating of three mafic samples, one acidic volcanic rock sample and one granitic sample yielded the concordia ages of ca. 400 Ma. Olivine chemical compositions indicate these mafic intrusions crystallized from evolved mafic magmas and compositions of the clinopyroxene and hornblende show typical arc affinities. Whole-rock compositions reveal their tholeiitic signature with enriched LREEs and LILEs and intensive depleted HFSEs (Nb, Ta, Zr and Hf), leading to low HFSE/LREE ratios (Nb/La = 0.1–0.4). Isotopically, these mafic intrusions have positive zircon $\varepsilon_{Hf}(t)$ (+7.6 to +14.3, mostly +10) and positive whole-rock $\varepsilon_{Nd}(t)$ (+0.8 to +5.3) values, which suggest that their parental magmas were derived from a time-integrated depleted mantle source. These features, together with the presence of primary water-bearing minerals (biotite and/or hornblende), suggest that their primitive magmas were derived from a time-integrated depleted lithosphere mantle which were metasomatized by fluids released from subduction slab. These findings, in combination with coeval voluminous granitoids and arc-signature volcanic rocks, indicate that the underplating of mafic magmas at the continental arc root leads to the partial melting of the continental crust. It is inferred that mafic magmatic underplating in the Altai orogenic belt significantly contributed to the Phanerozoic vertical continental crust growth in the Altai orogen.

1. Introduction

The Chinese Altai orogen is one of key parts of the Central Asian Orogenic Belt (CAOB), the largest Phanerozoic accretionary orogen in the world (Jahn et al., 2000a, b, 2004b; Şengör and Natalin, 1996;

et al., 2008; Zhang and Zou, 2013; Zhang et al., 2008a; Zhang et al., 2010a, 2010b, 2014). The early phase of ultramafic–mafic activity, however, is still poorly known (Cai et al., 2012).

In this study, we report detailed field observations, petrography, systematic zircon U–Pb ages and Hf isotope results, whole-rock major and trace element geochemistry, Sr–Nd isotope and mineral compositions for the Devonian gabbroic intrusions along the south Altai orogen, as well as zircon Hf isotope of the coeval granites and volcanic rocks. The objectives of this study are to (1) provide a better understanding of the petrogenesis of these gabboric intrusions and their tectonic background and (2) to evaluate the vertical continental growth of the Altai orogen.

2. Regional geology

The Central Asian Orogenic Belt (CAOB) extends 7000 km east to west, bounded in the north by the Siberia Craton and in the south by the Tarim Craton (Hu et al., 2000; Jahn et al., 2000a, b; Şengör et al., 1993; Windley et al., 2007; Xiao et al., 2009a) (Fig. 1a). The tectonic framework of the Chinese Altai section can be divided into three major units, i.e., the Altai orogenic belt (including Altai-Mongolian terrain and Rudny Altai terrain), the Irtish suture zone and the Junggar terrain (Xiao et al., 2009a; Yin et al., 2010; Zhang et al., 2012). Recent studies demonstrated that the basement of the Chinese segment of Altai-Mongolian terrain was formed during the Neoproterozoic to early Paleozoic rather than early Precambrian. As for the Junggar terrain, it was formed by multiple accretions of seamounts, intra-ocean arc, ophiolites fragments, and subduction complex from middle Cambrian to carboniferous (Chen and Jahn, 2004; Han et al., 2006; Jahn et al., 2004a; Xiao et al., 2004, 2009b; Zhang et al., 2009b). The Irtish belt, formed at ca 320 Ma, was regarded as the final suture zone between the Altai-Mongolian terrain and the Junggar terrain (Zhang et al., 2012).

Relative to the extensive distribution of granitoids along the southern margin of the Altai orogen, Devonian gabbroic intrusions in this area are of small volume. These gabbroic intrusions formed a NW–SE-trending belt (Fig. 1b), including, from east to west, the Keketuohai mafic–ultramafic complex (Cai et al., 2012), the Kuwei gabbroic intrusions and South Kuwei ultramafic–mafic complex, and the gabbroic and doleritic intrusions and dykes in Habahe area (Fig. 1b) (Xinjiang, 1993; Zhou et al., 2006).

3. Petrography

3.1. The Kuwei intrusion

In the Kuwei area, dozens of northwest-trending mafic intrusions (Figs. 1b and 2a) are emplaced in the middle-upper Ordovi-

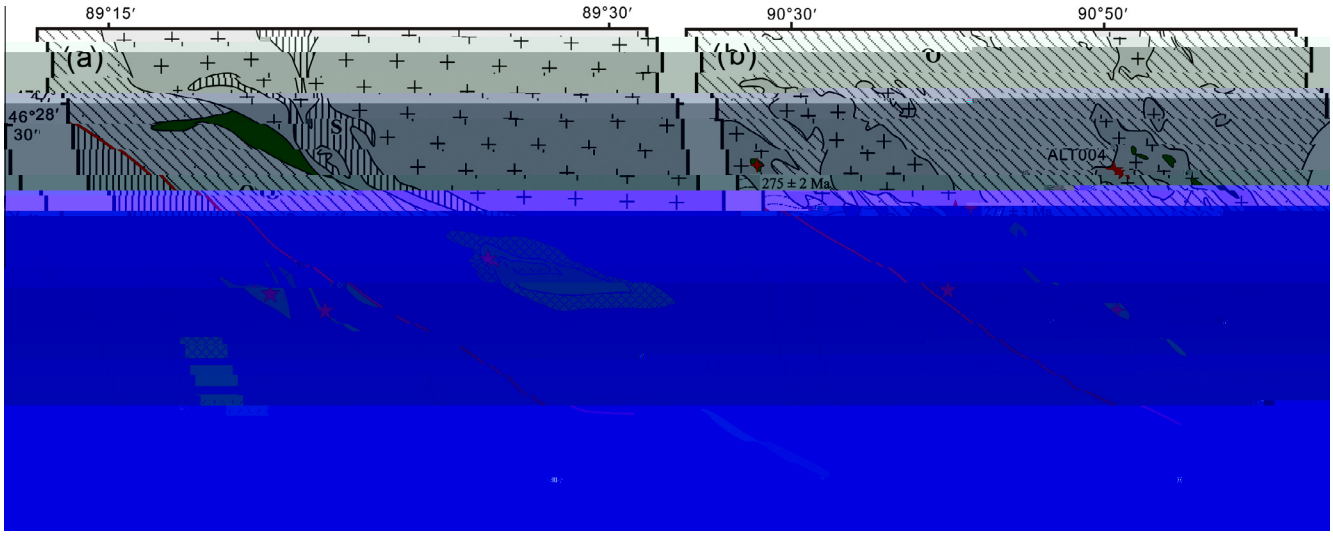

Fig. 2. (a) Geological map of the Kuwei intrusion and South Kuwei complex; (b) geological map of the Chaganguole granodiorite and the Mayinebo Formation, data from Zhang et al. (2010a).

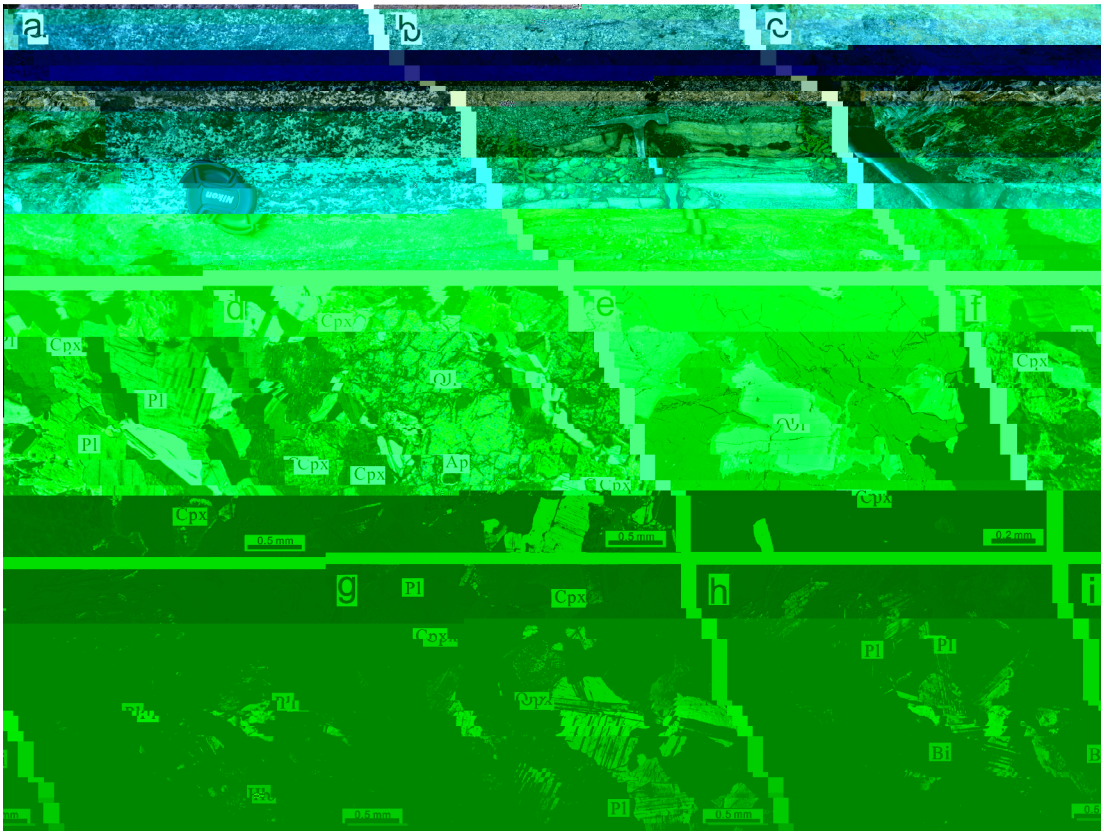

Fig. 3. Field photographs and microscopic photographs of gabbros from the Kuwei intrusion and the South Kuwei complex. (a) cumulate structure of the Kuwei intrusion; (b) intrusive contact between the South Kuwei complex; (c) phlogopite cystids in the South Kuwei complex; (d) sub-round olivine in the olivine-bearing gabbros (Kuwei intrusion); (e) olivine reaction rim of Kuwei gabbro; (f and g) typical gabbroic textures in gabbros (Kuwei intrusion); (h) biotite in the gabbros from the South Kuwei complex; (i) hornblende-bearing gabbro from the South Kuwei complex; Ap-apatite, Bi-biotite, Cpx-clinopyroxene, Hb-horblende, Ol-olivine, Opx-orthopyroxene, Pl-plagioclase.

mainly of 30% clinopyroxene, 10% orthopyroxene, 40% plagioclase and 15% hornblende. A gabbro sample (KW-1) from the Kuwei intrusion was collected for geochronological analyses.

3.2. The South Kuwei complex

The South Kuwei complex, located about 6 km west of the Kuwei intrusion, are also composed of dozens of small stocks, and intrude in the Silurian metamorphic volcanic–sedimentary sequences. The largest stock is about 2.5 km long and 0.1–1 km wide, which has a roughly elliptical shape and shows sharp contact with a granitic batholith in the southwest. No chilled margins were observed (Figs. 2a and 3b).

The dominant rocks of the South Kuwei complex are gabbro and hornblende gabbro with minor biotite (or phlogopite)-rich gabbro. At several places, stripes of dozens square centimeters are

observed (Fig. 3c). The phlogopite crystallized from water-rich residual mafic magma (e.g., Ye et al., 2013). Most rocks from the South Kuwei complex exhibit coarse- to medium-grained texture. The hornblende and biotite fill into the spaces between the semi-euhedral pyroxene and/or plagioclase (Fig. 3h and i). Gabbro contains 35–45% clinopyroxene, 10–15% orthopyroxene, 40–45% plagioclase and ~5% opaque minerals. Hornblende-bearing gabbro consists mainly of 45% clinopyroxene, 10% orthopyroxene, 40% plagioclase and less 5% hornblende and biotite. Two hornblende-bearing gabbro samples from the South Kuwei complex were collected for geochronological analyses.

3.3. The Chaganguole granodiorite pluton and Mayinebo Formation

The Chaganguole granodiorite pluton is located northeast of the Mayinebo fault and intrudes in Ordovician Habahe Group (Fig. 2b). Main rock types include granite and granodiorite and the main body is ~12 km long and ~4 km wide. Fine- to medium-grained gabbro enclaves with 0.2–0.5 m × 0.2–0.5 m in dimensions, intermingled with the granite and granodiorite, are commonly observed. Granodiorite from the pluton is medium-grained and the principal minerals comprise quartz (20–25%), hornblende (20–30%), plagioclase (60–70%) and biotite (1–5%). Accessory minerals include zircon and apatite. A granodiorite sample (ALT004) from the Chaganguole pluton was collected for zircon U–Pb and Hf isotope analyses.

The Mayinebo Formation has a limited distribution in the eastern Altai orogen, which occurs to the east of Fuyun fault and just on the northeast of the Mayinebo fault (Figs. 1b and 2b). It consists of sandstone, siltstone, and acidic volcanic rocks, and the units near Mayinebo fault were converted into biotite-schists and leptites after regional metamorphism. The 5–6 m thick biotite-schists have several 3–3.5 m thick leptites interbeds. One acidic volcanic rock sample was collected for zircon U–Pb dating and Hf isotope analyses.

4. Analytical methods

Zircon grains were separated using conventional heavy liquid and magnetic techniques, hand-picked under a binocular microscope and representative grains were mounted in an epoxy resin disk, and then polished to section the crystals for analysis. Zircons were photographed in transmitted and reflected light micrographs as well as cathodoluminescence (CL) images to reveal their internal structures. Zircon U–Pb dating and Hf isotope analyses were carried out using the LA–MC–ICPMS method at Tianjin Institute of Geology and Mineral Resources. The detailed analytical procedures have been documented in Hou et al. (2009), Geng et al. (2001). Software SQUID 1.0 and ISOPLOT (Ludwig, 1999, 2001) were used for data processing. The weighted mean ages are quoted at 95% confidence level. Zircon U–Pb age data are listed in supplementary Table 1.

Hf isotopic analyses were carried on the same zircon grains that were previously analyzed for U–Pb ages, using a Neptune MC-ICPMS, equipped with a 193 nm laser, at Tianjin Institute of Geology and Mineral Resources. During analyses, a laser repetition rate of 10 Hz at 100 mJ was used and spot size was 63 μm. The detailed analytical procedures were similar to those described by Wu et al. (2006). Zircon Hf isotope data are presented in supplementary Table 2.

Mineral compositions of olivine, clinopyroxene, and hornblende were determined by wavelength-dispersion X-ray emission spectrometry using an EPMA-1600 electron microprobe at the State Key Laboratory of Isotope Geochemistry, Guangzhou Institute of Geochemistry, Chinese Academy of Sciences. Operating conditions were 15 keV accelerating voltage and 15 nA beam current with 20 s counting time. Representative mineralogical data are listed in supplementary Tables 3–5.

Major elements were measured by Rigaku ZSX100e X-ray fluorescence spectrometer (XRF) at the State Key Laboratory of Isotope Geochemistry, Guangzhou Institute of Geochemistry, Chinese Academy of Sciences, using fused lithium-tetraborate glass pellets. Analytical precision as determined on the Chinese National standard GSR-1 and GSR-3 were generally better than 2%. Trace elements were analyzed using a Perkin–Elmer Sciex ELAN 6000 ICPMS at the State Key Laboratory of Isotope Geochemistry, Guangzhou Institute of Geochemistry, Chinese Academy of Sciences, following procedures described by Li et al. (2004). The analytical precision for most elements was better than 3–5%. The analytical results are presented in Table 1.

Whole-rock Nd–Sr isotopic measurements were spiked and dissolved in Teflon bombs with HF + HNO_3 acid, and then separated by conventional cation-exchange techniques. The isotopic measurements were performed on a Micromass Isoprobe multi-collector inductively coupled plasma mass spectrometry (MC-ICPMS) at Yichang Institute of Geology and Mineral Resources, following the procedure described by Li et al. (2004). The measured $^{87}Sr/^{86}Sr$ and $^{143}Nd/^{144}Nd$ ratios are normalized to $^{86}Sr/^{88}Sr = 0.1194$ and $^{146}Nd/^{144}Nd = 0.7219$, respectively. The report $^{87}Sr/^{86}Sr$ and $^{143}Nd/^{144}$

Zircon Sample ALT3

Table 1
Geochemical compositions of the Kuwei intrusion and South Kuwei complex.

*Samples from the Kuwei intrusion

Sample	Gabbro							Olivine-bearing gabbro			
	ALT035H1	ALT035H2	ALT035H3	ALT035H4	ALT035H5	ALT035H6	ALT035H7	ALT036H1	ALT036H2	ALT036H3	ALT036H4
Major elements (%)											
SiO_2	45.86	45.97	44.95	45.12	45.90	46.96	45.32	44.71	46.59	45.84	47.28
TiO_2	0.40	0.51	0.43	0.79	0.80	0.33	0.22	0.11	0.20	0.15	0.41
Al_2O_3	14.96	17.92	15.45	17.34	16.52	18.68	22.00	19.87	21.93	21.87	20.64
$Fe_2O_3^T$	9.37	9.67	10.49	11.59	12.33	6.80	7.08	8.37	5.39	6.49	6.84
MnO	0.15	0.15	0.15	0.15	0.17	0.12	0.11	0.12	0.09	0.10	0.11
MgO	11.36	9.87	12.74	8.97	9.96	8.98	8.24	13.08	8.40	9.42	8.67
CaO	15.47	14.41	12.91	13.76	11.77	16.85	14.68	12.59	15.98	14.76	13.96
Na_2O	0.14	0.42	0.48	0.27	0.92	0.43	0.42	0.30	0.60	0.50	0.64
K_2O	0.05	0.01	0.07	0.07	0.13	0.01	0.05	0.01	0.02	0.02	0.07
P_2O_5	0.00	0.01	0.00	0.00	0.00	0.01	0.00	0.00	0.01	0.00	0.01
LOI	1.89	0.44	1.94	1.39	1.46	0.53	1.52	0.02	0.25	0.30	1.11
Total	99.65	99.36	99.61	99.46	99.97	99.69	99.64	99.17	99.45	99.46	99.74
$Mg^{\#}$	70.6	66.9	70.6	60.5	61.5	72.3	69.7	75.6	75.5	74.2	71.5
Trace elements (ppm)											
Sc	98.7	73.2	62.3	84.5	64.6	92.4	43.4	31.9	47.7	42.0	57.4
V	428	487	387	800	793	312	230	124	197	179	296
Cr	856	414	708	359	277	700	427	461	605	443	396
Co	63.9	76.3	85.9	68.6	70.8	55.1	57.4	84.4	45.4	61.1	54.0
Ni	152	134	323	67	140	125	110	250	112	136	85.7
Ga	16.7	20.7	19.8	20.6	23.3	20.7	20.9	17.7	18.4	19.1	20.4
Rb	1.28	0.83	2.53	1.51	3.11	0.97	1.44	1.01	1.63	1.53	2.56
Sr	210	240	141	239	223	257	279	245	259	261	251
Y	6.24	4.91	7.61	5.00	5.32	6.09	3.23	2.13	3.66	3.25	6.51
Zr	8.66	7.98	11.3	7.07	11.5	9.52	5.42	4.70	6.48	6.60	13.5
Nb	0.18	0.25	0.24	0.12	0.34	0.22	0.16	0.15	0.18	0.15	0.66
Ba	14.2	15.3	35.7	18.1	52.7	23.7	32.1	13.0	16.1	0.06	0.22
La	0.99	1.17	1.36	0.76	1.77	1.83	1.16	0.93	1.10	22.2	24.9
Ce	2.83	2.96	3.91	2.05	4.21	3.95	2.74	2.01	2.69	1.45	2.09
Pr	0.49	0.47	0.60	0.33	0.60	0.68	0.43	0.27	0.40	3.26	5.81
Nd	2.75	2.75	3.46	2.00	3.02	3.61	2.09	1.28	2.00	0.44	0.84
Sm	1.04	0.93	1.36	0.74	0.95	1.16	0.71	0.38	0.67	2.03	4.18
Eu	0.47	0.59	0.65	0.42	0.50	0.54	0.48	0.29	0.40	0.57	1.26
Gd	1.19	1.03	1.42	0.89	1.00	1.21	0.64	0.39	0.67	0.40	0.56
Tb	0.17	0.15	0.22	0.13	0.14	0.19	0.10	0.05	0.10	0.60	1.28
Dy	1.33	1.09	1.70	0.97	1.12	1.30	0.68	0.42	0.70	0.09	0.18
Ho	0.33	0.31	0.46	0.26	0.30	0.35	0.19	0.12	0.18	0.68	1.35
Er	0.80	0.77	1.21	0.71	0.77	0.88	0.50	0.33	0.54	0.19	0.34
Tm	0.12	0.11	0.16	0.09	0.11	0.12	0.07	0.04	0.07	0.48	0.93
Yb	0.66	0.67	1.02	0.56	0.71	0.71	0.42	0.29	0.45	0.07	0.13
Lu	0.10	0.11	0.16	0.08	0.12	0.11	0.06	0.04	0.07	0.42	0.83
Hf	0.40	0.46	0.69	0.38	0.54	0.53	0.28	0.23	0.30	0.08	0.12
Ta	0.02	0.03	0.03	0.02	0.03	0.02	0.02	0.01	0.02	0.28	0.65
Th	0.13	0.10	0.14	0.03	0.13	0.38	0.10	0.14	0.12	0.02	0.04
U	0.02	0.10	0.17	0.02	0.05	0.03	0.03	0.03	0.06	0.34	0.24

*Samples from the South Kuwei complex

Sample	Gabbro			Hornblende-bearing gabbro								
	ALT037H1	ALT037H2	ALT038H1	ALT038H2	ALT038H3	ALT038H4	ALT038H4	ALT038H5	ALT038H6	ALT039H2	ALT039H3	ALT039H4	ALT039H5
Major elements (%)													
SiO_2	47.53	48.37	46.98	48.95	44.52	49.03	48.50	50.68	50.18	48.87	49.06	48.48	49.62
TiO_2	0.79	0.79	0.81	0.62	0.30	0.59	0.49	0.59	0.64	0.63	0.69	0.92	0.78
Al_2O_3	18.88	19.01	18.59	16.97	17.66	16.52	16.97	15.90	16.49	18.13	18.04	16.61	16.98
$Fe_2O_3^T$	9.86	9.86	9.30	7.85	7.88	7.84	7.71	6.45	7.51	7.33	7.07	8.87	8.06
MnO	0.13	0.11	0.14	0.14	0.12	0.14	0.13	0.11	0.14	0.13	0.13	0.15	0.14
MgO	6.88	6.95	6.27	9.64	14.01	9.92	10.12	9.53	9.13	9.08	9.49	9.22	9.49
CaO	12.13	11.16	13.56	11.63	10.43	11.69	12.40	12.27	11.66	10.95	11.10	11.44	10.27
Na_2O	1.35	1.97	1.69	1.36	0.90	1.27	1.27	1.15	1.74	2.01	1.54	1.54	1.87
K_2O	0.16	0.19	0.19	0.22	0.47	0.21	0.23	0.36	0.16	0.22	0.21	0.21	0.17
P_2O_5	0.19	0.16	0.15	0.06	0.03	0.05	0.03	0.03	0.04	0.06	0.05	0.06	0.06
LOI	1.06	0.95	1.31	1.98	3.08	2.01	1.52	2.04	1.64	1.86	1.52	1.68	2.07
Total	98.96	99.52	98.99	99.41	99.39	99.27	99.38	99.11	99.33	99.26	98.90	99.18	99.51
$Mg^{\#}$	58.0	58.3	57.2	70.9	77.9	71.5	72.2	74.5	70.7	71.0	72.7	67.3	70.0
Trace elements (ppm)													
Sc	36.7	35.1	31.5	42.4	24.4	61.5	55.7	60.5	59.5	41.7	45.1	54.0	48.2
V	495	445	395	261	168	377	329	368	368	297	303	393	337
Cr	36.5	24.8	25.5	474	360	640	508	645	306	469	886	401	739
Co	52.9	52.2	49.3	47.6	77.8	55.9	61.1	48.5	46.2	52.3	46.6	56.2	52.8
Ni	71.6	66.4	61.5	155	380	185	186	176	120	209	131	141	124

(*continued on next page*)

Table 1 (*continued*)

*Samples from the South Kuwei complex													
Sample	Gabbro			Hornblende-bearing gabbro									
	ALT037H1	ALT037H2	ALT038H1	ALT038H2	ALT038H3	ALT038H4	ALT038H4	ALT038H5	ALT038H6	ALT039H2	ALT039H3	ALT039H4	ALT039H5
Ga	25.3	24.3	22.7	18.6	17.9	21.1	20.6	19.8	22.1	20.4	21.7	22.7	22.3
Rb	2.90	3.56	2.36	9.01	26.25	9.05	7.59	17.3	6.18	7.22	8.52	6.88	6.70
Sr	427	432	469	238	251	231	234	220	247	161	159	143	149
Y	13.4	13.0	13.8	12.3	5.69	12.8	10.1	14.2	13.4	14.1	14.1	20.1	18.4
Zr	40.9	40.9	42.6	51.7	26.8	51.8	45.8	43.3	39.7	45.4	33.6	55.2	13.4
Nb	1.92	2.46	2.37	1.16	0.77	1.17	0.74	1.48	0.90	1.29	1.04	1.66	1.38
Ba	159	155	87.6	64.5	95.8	114	142	143	350	126	56.8	88.9	82.9
La	6.70	6.52	5.92	5.78	3.67	6.42	4.99	7.53	5.46	4.70	3.48	4.65	4.77
Ce	15.86	15.28	14.21	14.04	8.91	16.10	13.03	17.79	13.99	10.63	8.65	12.36	12.33
Pr	2.20	2.14	2.05	2.03	1.23	2.30	1.88	2.43	2.11	1.56	1.36	1.84	1.84
Nd	10.49	10.55	9.70	9.33	5.47	11.11	8.85	11.26	10.45	7.92	7.29	9.49	9.74
Sm	2.93	3.03	2.72	2.68	1.49	2.96	2.47	3.39	3.05	2.53	2.45	3.35	3.07
Eu	1.28	1.15	1.10	0.97	0.60	1.11	0.98	1.08	1.24	0.99	1.06	1.32	1.24
Gd	2.94	2.72	2.63	2.32	1.22	2.58	2.20	2.86	2.73	2.58	2.52	3.59	3.27
Tb	0.42	0.41	0.37	0.33	0.18	0.36	0.31	0.42	0.41	0.39	0.38	0.55	0.48
Dy	2.93	2.72	2.80	2.36	1.19	2.59	2.30	3.02	2.73	3.00	2.91	4.07	3.56
Ho	0.78	0.71	0.71	0.60	0.31	0.69	0.59	0.79	0.73	0.75	0.74	1.08	0.98
Er	2.01	1.93	1.89	1.62	0.87	1.92	1.60	2.17	2.06	2.14	2.13	3.02	2.65
Tm	0.29	0.26	0.27	0.23	0.12	0.25	0.23	0.29	0.27	0.29	0.29	0.40	0.35
Yb	1.83	1.71	1.68	1.56	0.80	1.66	1.45	1.90	1.83	1.87	1.84	2.62	2.30
Lu	0.29	0.26	0.28	0.23	0.13	0.27	0.25	0.30	0.28	0.31	0.29	0.41	0.38
Hf	1.66	1.52	1.58	1.86	1.06	2.11	1.75	2.03	1.69	1.86	1.57	2.36	1.13
Ta	0.15	0.17	0.16	0.11	0.06	0.09	0.06	0.15	0.07	0.10	0.07	0.35	0.09
Th	0.55	0.50	0.47	1.34	0.84	1.42	1.15	2.86	0.99	1.13	0.35	0.53	0.78
U	0.25	0.28	0.23	0.37	0.29	0.39	0.30	0.71	0.30	0.28	0.11	0.17	0.18

Table 2
Sr–Nd isotopic compositions of the gabbros.

Sample	Rock type	Rb (ppm)	Sr (ppm)	$^{87}Rb/^{86}Sr$	$^{87}Sr/^{86}Sr$ (2σ)	$(^{87}Sr/^{86}Sr)_i$	Sm (ppm)	Nd (ppm)	$^{147}Sm/^{144}Nd$	$^{143}Nd/^{144}Nd$ (1σ)	$(^{143}Nd/^{144}Nd)_i$	ε_{Nd} (T)
Kuwei intrusion												
ALT035H3	gabbro	1.83	138	0.0382	0.705520 (4)	0.705313	0.895	2.46	0.2205	0.512812 (6)	0.512262	2.2
ALT035H4	gabbro	0.965	226	0.0123	0.705742 (2)	0.705673	0.628	1.75	0.2167	0.512746 (9)	0.512205	1.1
ALT035H5	gabbro	1.18	201	0.0170	0.705901 (5)	0.705808	0.617	1.91	0.1955	0.512674 (6)	0.512186	0.8
ALT035H6	gabbro	0.406	236	0.00485	0.705712 (3)	0.705684	0.767	2.13	0.2176	0.512753 (8)	0.512210	1.2
ALT035H7	gabbro	0.982	259	0.0109	0.705664 (2)	0.705601	0.442	1.43	0.1875	0.512690 (7)	0.512222	1.5
ALT036H1	gabbro	0.491	235	0.00603	0.705491 (6)	0.705457	0.251	0.848	0.1790	0.512698 (5)	0.512251	2.0
ALT036H3	gabbro	0.960	252	0.0110	0.70529 5(4)	0.705230	0.417	1.51	0.1672	0.512675 (9)	0.512258	2.2
South Kuwei complex												
ALT038H2	gabbro	18.3	237	0.223	0.705501 (2)	0.704232	0.941	3.82	0.1491	0.512712 (5)	0.512321	3.9
ALT038H6	gabbro	4.10	221	0.0536	0.704682 (4)	0.704375	2.02	7.42	0.1649	0.512826 (8)	0.512394	5.3
ALT039H3	gabbro	6.25	146	0.124	0.705214 (4)	0.704505	1.73	5.44	0.1922	0.512812 (6)	0.512309	3.6

$\varepsilon_{Nd}(t) = 10{,}000[(^{143}Nd/^{144}Nd)_S(t)/(^{143}Nd/^{144}Nd)_{CHUR}(t) - 1]$; $\varepsilon_{Nd}(t)$ and $(^{87}Sr/^{86}Sr)_i$ values of Kuwei gabbros are recalculated using the age of 381 Ma, South Kuwei gabbros are recalculated using the age of 400 Ma.

142 ppm and from 25 ppm to 114 ppm, respectively, with Th/U ratios from 0.32 to 0.95. All the analyses form a tight cluster on concordia plot within analytical errors (Fig. 4c). The weighted mean of $^{206}Pb/^{238}U$ ages gives a weighted value of 398.7 ± 1.8 Ma (95% confidence interval, MSWD = 3.1). Thus, the ages of ca. 400 were interpreted as the crystallization age of the South Kuwei complex.

5.1.3. The Chaganguole granodiorite pluton (granodiorite sample ALT004: N46°28′10″, E90°48′37″)

Zircons from the sample ALT004 are transparent and subeuhedral, ranging from 80 to 150 μm long with aspect ratio of 1–2. These zircons show relative homogenous inner structure with slightly bright CL images (see insert of Fig. 4d). Twenty-two analyses conducted on 22 zircons (supplementary Table 1) yield variable U and Th contents (U = 84–232 ppm, Th = 50–190 ppm, Th/U = 0.37–0.89). Their $^{206}Pb/^{238}U$ ages are consistent within analytical errors and yield a weighted mean $^{206}Pb/^{238}U$ age of 394.0 ± 3.6 Ma (Fig. 4d) (95% confidence interval, MSWD = 0.91).

5.1.4. The Mayinebo Formation (sample ALT001: N46°21′13″, E90°33′43″)

Zircons are mostly clear, euhedral prismatic grains with concentric zonings in CL images (see insert of Fig. 4e), about 100 μm long with aspect ratio of 2–3. Thirty analyses were performed on 30 zircon grains (supplementary Table 1). The analyses show variable abundance of U (128–1798 ppm) and Th (72–834 ppm) and Th/U ratios of 0.25–1.04. All analyses are concordant within analytical errors, and give a weighted mean $^{206}Pb/^{238}U$ age of 400.8 ± 3.6 Ma (Fig. 4e) (95% confidence interval, MSWD = 1.3). This age is regarded as the eruption age of acid volcanic rocks in the Mayinebo Formation.

To summarize the above age results, the weighted mean $^{206}Pb/^{238}U$ ages for gabbros from the Kuwei intrusion and hornblende-bearing gabbros from the South Kuwei complex are 381.2 ± 2.8 Ma and ca. 400 Ma, respectively (Fig. 4f). The zircon U–Pb age for granodiorite from the Chaganguole granodiorite pluton and leptite from Mayinebo Formation are also ca. 400 Ma, consistent with previous geochronological data of the meta-felsic volcanic rocks and tuffs in Kangbutiebao Formation (Chai et al.,

2006, 2012a, 2012b and references therein). These results suggest that the igneous rocks and metavolcanic rocks were formed at 380–400 Ma along the southern Altai orogen (Fig. 4f).

5.2. Minerals chemical compositions

5.2.1. Olivine

Chemical compositions of olivine grains from the Kuwei gabbros and South Kuwei gabbros are listed in supplementary Table 3. These olivines have MnO ranging from 0.21 to 0.43 wt.%, and NiO from 0.02 to 0.74 wt.%. The olivines are chemically homogeneous, with Forsterite (Fo) ranging from 78 to 81, which is similar to the olivine of dunites from the Alaskan-type mafic–ultramafic complex (Irvine, 1974).

5.2.2. Pyroxene

Clinopyroxenes have SiO_2 ranging from 50.03 to 52.76 wt.%, CaO from 16.31 to 23.54 wt.%, TiO_2 from 0.35 to 1.01 wt.%, Al_2O_3 from 2.21 to 4.26 wt.%, FeO from 6.34 to 11.12 wt.%, and Na_2O from 0.17 to 0.51 wt.%. Twenty-five clinopyroxene grains and three clinopyroxenes reported by Zhang et al. (2008b) exhibit similar high $Mg^{\#}$ (74–87). These clinopyroxenes are characterized by high Ca and low Ti, Al and Na, and plot into the diopside field in the Wo–En–Fs diagram (Fig. 5a), which resembles those clinopyroxenes from Alaskan-type complex (Snoke et al., 1981; Helmy and El Mahallawi, 2003). Furthermore, they define a clear arc cumulates trend in the Al^{VI} vs. TiO_2 diagram (Fig. 5b and c, after Loucks, 1990).

Eight orthopyroxene grains from the Kuwai intrusion and five orthopyroxene grains from South Kuwai complex were analyzed for chemical compositions (supplementary Table 4). They have relatively high MgO (22.50–30.64 wt.%) with $Mg^{\#}$ ranging from 66 to 85 and low TiO_2 (0.17 and 0.28 wt.%), Al_2O_3 (2.06 and 2.21 wt.%), and CaO (0.80 and 0.92 wt.%). They plot into the field of clinoenstatite in the Wo–En–Fs diagram (Fig. 5a).

5.2.3. Hornblende

Primary hornblendes from the gabbros of the Kuwei intrusion

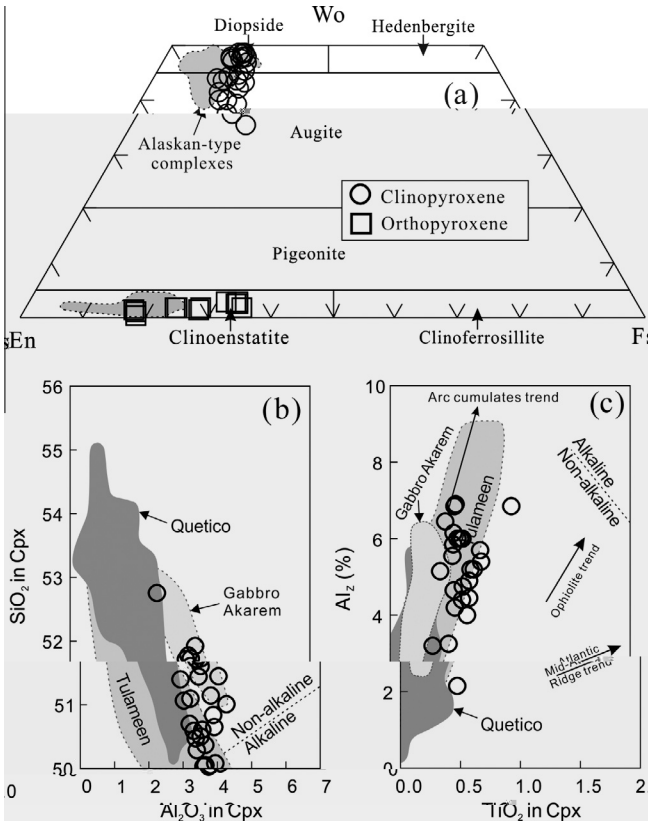

Fig. 5. (a) Wo–En–Fs diagram showing the compositions of the clinopyroxene from the Kuwei intrusion; (b) Al_2O_3 (wt.%) vs. $TiO_2 + Cr_2O_3$ (wt.%) and Al_{IV} (percentage of tetrahedral site occupied by Al_Z) vs. TiO_2 (wt.%) in clinopyroxene from the Kuwei intrusion. The gray fields are modified from Su et al. (2013), reference lines of arc-related and rift-related tectonic environments are from Loucks (1990).

ALT05B2) are sub-alkalic affinity (ANa + AK less than 0.5) and classified as magnesio-hornblende and tschermakitic-hornblende (Fig. 6a). Although the investigated primary hornblendes display a grater range of major oxides (supplementary Table 5), their low alkali and high Mg are similar to those of hornblendes from mafic rocks of Alaskan-type complex (e.g. Helmy and El Mahallawi, 2003) and show significant arc affiliates (Fig. 6b).

5.3. Whole-rock elemental geochemistry

Major and trace elements concentrations of representative gabbros from the Kuwei intrusion and South Kuwei complex are presented in Table 1.

5.3.1. The Kuwei intrusion

The gabbros from the Kuwei intrusion have SiO_2 contents ranging from 45.1 to 47.9 wt.%, and variable other oxides and compatible elements (e.g., Cr, Ni, V) (see Table 1). They are characterized by extremely low total alkali contents (less than 1%) and exhibit tholeiitic trend in AFM ($Na_2O + K_2O$–FeO–MgO) diagram (Fig. 7). In Harker diagrams (Fig. 8), as $Mg^{\#}$ decreases from 76 to 61, SiO_2, Fe_2O_3, TiO_2, P_2O_5, Zr and Y increase while Al_2O_3, CaO, Cr and Ni decrease, but Na_2O and K_2O are not correlated with $Mg^{\#}$.

The Kuwei gabbros have lower total REE contents (6.8–20 ppm). On the chondrite-normalized patterns (Chondrite and primitive mantle values are from Boynton (1984) and Sun and McDonough (1989), respectively), they show slight LREE-enriched patterns with $(La/Yb)_N$ ranging from 1.0 to 2.5 and significant positive Eu anomalies ($\delta Eu = 1.3–2.3$), suggesting plagioclase cumulation (Fig. 9a). Normalized to primitive mantle, all samples show variable enrichments in LILEs, significant Nb–Ta and P trough (Nb/La = 0.11–0.31) and Sr–Ba hump (Fig. 9b). The positive Sr anomalies are concurrent with the positive Eu anomalies, indicating plagioclase accumulation.

5.3.2. The South Kuwei complex

The gabbros from the South Kuwei complex have SiO_2 content ranging from 48.1 to 52.2 wt.%, but large range of compatible trace element contents (Cr = 25–886 ppm, Ni = 61–380 ppm) (Table 1). Their $Mg^{\#}$ values range from 57 to 78. In the AFM ($Na_2O + K_2O$–FeO–MgO) diagram, the rocks follow a tholeiitic trend (Fig. 7). On the Harker diagrams, as $Mg^{\#}$ decreases, SiO_2, Fe_2O_3, TiO_2, Na_2O, K_2O, P_2O_5, Zr and Y increase while Al_2O_3, CaO, Cr and Ni decrease (Fig. 8).

The gabbro samples have low total REE abundances (26–55 ppm). Their Chondrite-normalized patterns exhibit slightly enrichment of LREE ($(La/Yb)_N = 1.3–3.3$) and broadly flat HREE ($(Gd/Yb)_N = 1.1–1.3$) patterns with slightly negative to variable positive Eu anomalies ($\delta Eu = 0.9–1.3$) (Fig. 9c). On the primitive mantle normalized spider diagrams, they are extremely depleted in Nb, Ta with Nb/La ratios from 0.15 to 0.40 and variable enriched Sr and Ba relative to their adjacent elements (Fig. 9d).

5.4. Whole-rock Sr–Nd isotopic compositions

Strontium and neodymium isotopic compositions of the representative gabbros are listed in Table 2. The samples from the Kuwei intrusion show a narrow range of $^{87}Rb/^{86}Sr$ ratios (0.004854–0.03817) and $^{87}Sr/^{86}Sr$ ratios (0.7053–0.7059), corresponding to relatively homogeneous initial $^{87}Sr/^{86}Sr$ ratios (0.7052–0.7058), slightly higher than that of primitive mantle (0.7047). As for neodymium isotope compositions, they have $^{147}Sm/^{144}Nd$ ratios between 0.1790 and 0.2205 and $^{143}Nd/^{144}Nd$ ratios between

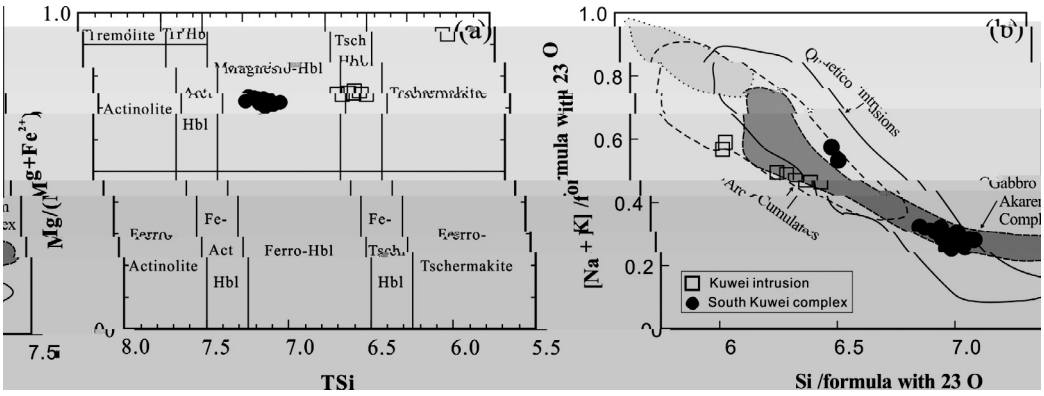

Fig. 6. (a) Hornblende classification after Leake et al. (1997); (b) Na + K vs. Si in hornblende after Pettigrew and Hattori (2006).

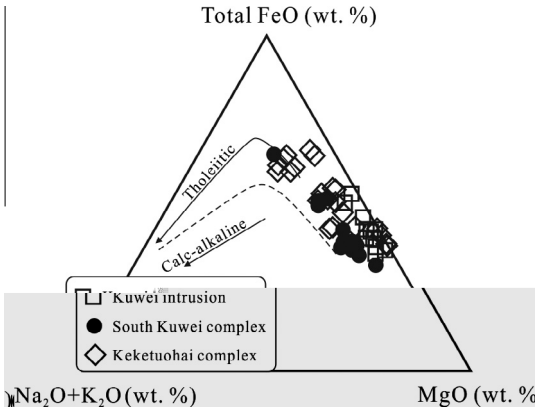

Fig. 7. AFM diagram ($A = Na_2O + K_2O$, $F = FeO$ (recalculated after the formula $FeO = 0.8998 * Fe_2O_3$), $M = MgO$) for gabbros from the Kuwei intrusion and South Kuwei complex showing their tholeiitic trend, Keketuohai data are from Cai et al. (2012).

0.512674 and 0.512812 and a nearly constant $\varepsilon_{Nd}(t)$ values from + 0.8 to + 2.2. In contrast to the Kuwei intrusion, the three representative gabbro samples from the South Kuwei complex have nearly identical initial $^{87}Sr/^{86}Sr$ ratios (about 0.7043) and high initial $\varepsilon_{Nd}(t)$ values varying from +3.6 to +5.3. All studied samples exhibit positive $\varepsilon_{Nd}(t)$ and low $(^{87}Sr/^{86}Sr)_i$ values, suggesting that the parental magmas to the gabbros were derived from a time-integrated depleted mantle source (Fig. 10).

5.5. Zircon Lu–Hf isotopes

Zircons from the South Kuwei complex (ALT038 and ALT039) show a narrow range of initial $^{176}Hf/^{177}Hf$ ratios (0.282752–0.282942), corresponding to $\varepsilon_{Hf}(t)$ values ranging from +7.6 to +14.3 (Fig. 11a), mostly at +10, which are slightly lower than other coeval mafic rocks along southern Altai orogen (Cai et al., 2010; Yao et al., 2013) (Fig. 11b). The zircons from the silicic meta-volcanic rock sample (ALT004) have a range of initial $^{176}Hf/^{177}Hf$ ratios from 0.282608 to 0.282683, corresponding to $\varepsilon_{Hf}(t)$ values between +2.7 and +5.4 (mostly about +4) (Fig. 11c), which are similar to other granitoids from the southern Altai orogen (Cai et al., 2011b, 2011c; Liu et al., 2012; Sun et al., 2008, 2009; Wang et al., 2011) (Fig. 11d).

6. Discussion

The close spatial, temporal relationship and similar elemental features of the Kuwei intrusion and South Kuwei complex, suggest that they possibly share a common mantle source and magma evolution process at the same tectonic setting.

6.1. Crustal contamination

The gabbro samples from the Kuwei intrusion and South Kuwei complex have well preserved primary minerals. With the exception

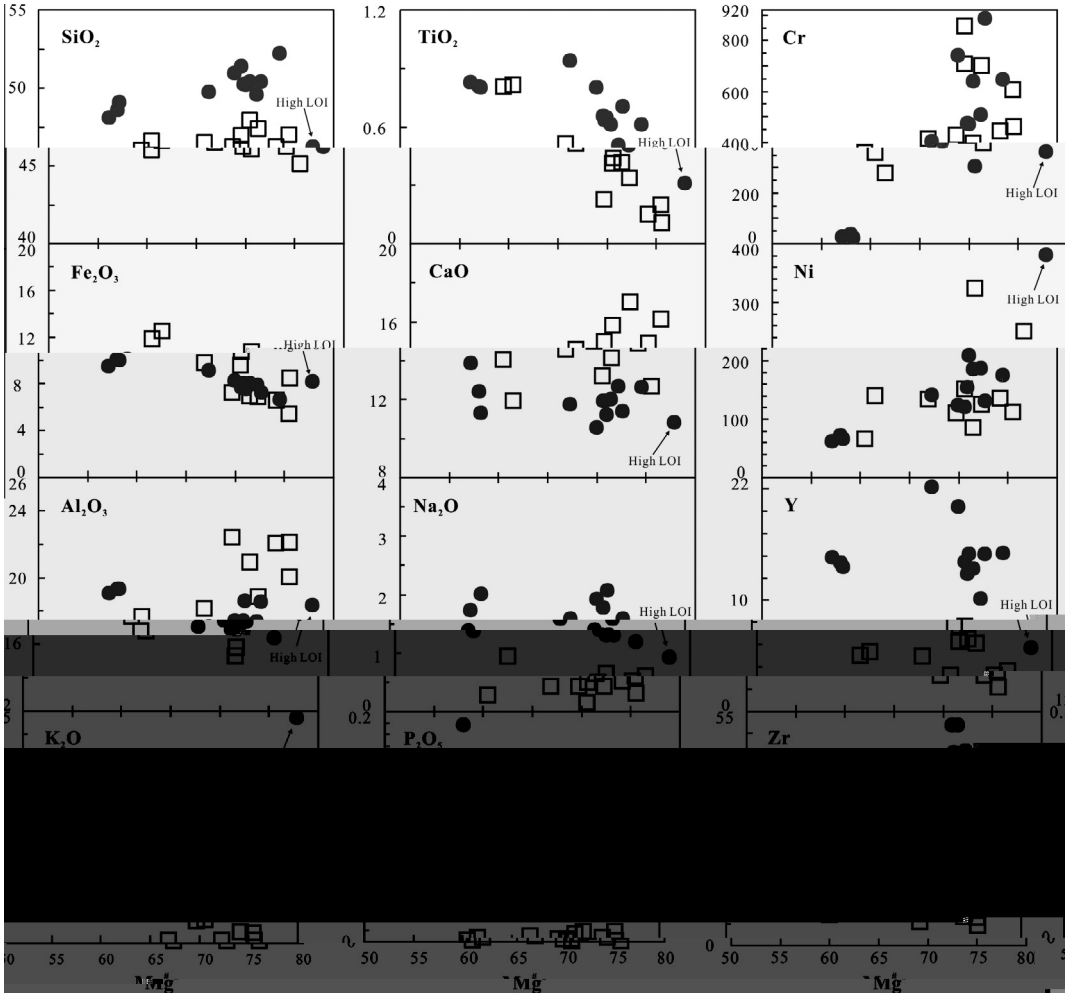

Fig. 8. Binary variation diagrams ($Mg^{\#}$ vs. SiO_2, Fe_2O_3, Al_2O_3, K_2O, TiO_2, CaO, Na_2O, P_2O_5, Cr, Ni, Y, and Zr) for gabbros from the Kuwei intrusion and South Kuwei complex. $Mg^{\#} = MgO/(MgO + FeO^T)$ in molecular ratio, $FeO^T = 0.8998Fe_2O_3^T$ (symbols are the same as in Fig. 6).

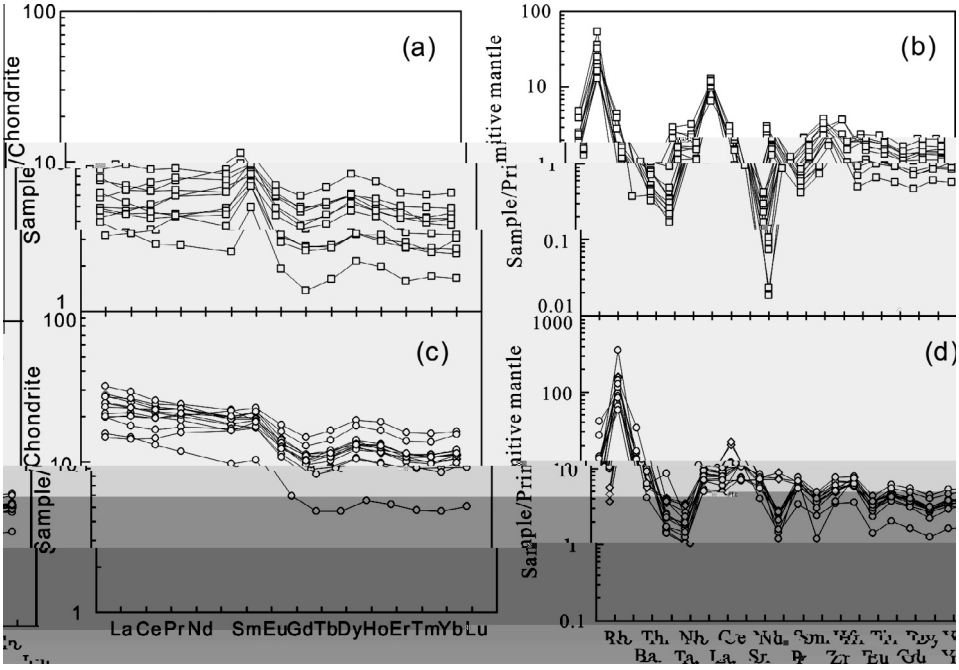

Fig. 9. Chondrite-normalized rare earth element (REE) patterns and primitive mantle-normalized trace-element spider diagrams for gabbro samples from the Kuwei intrusion (a and b) and South Kuwei complex (c and d), respectively. Chondrite-normalizing values are from Boynton (1984), primitive mantle-normalizing values are from Sun and McDonough (1989).

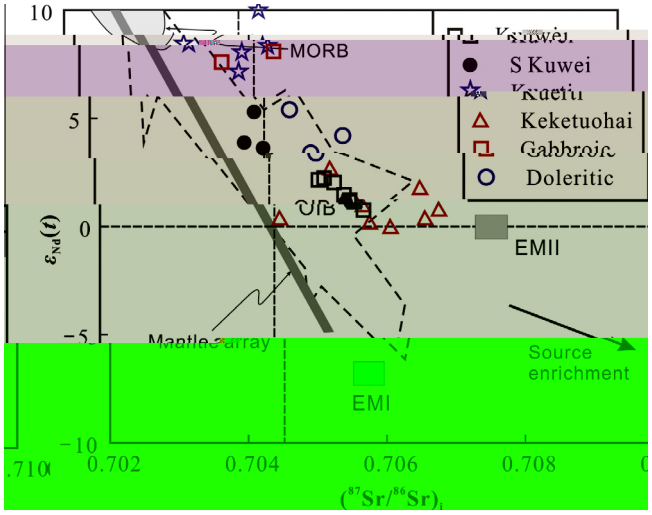

Fig. 10. $\varepsilon_{Nd}(t)$ vs. $(^{87}Sr/^{86}Sr)_i$ diagram for the Kuwei intrusion and South Kuwei complex along the southern Altai orogen. MORB field is from Zimmer et al. (1995), OIB field is from White and Duncan (1996), EMI and EMII are from Hart (1988). Data for Kuerti mafic rocks are from Xu et al. (2003), data for Keketuohai mafic–ultramaifc rocks are from Cai et al. (2012), and data for gabbroic and doleritic dykes are from Cai et al. (2010).

of sample ALT038H2 from the South Kuwei complex, all gabbro samples have low loss-on-ignition (LOI) less than 2.0 wt.%.

Generally, crustal contamination could diminish Nb/La, Ta/La and Nb/Th ratios and elevate Th/Yb ratios (Neal et al., 2002; Pearce, 2008). Strictly speaking, trace elements approach is more applicable to basalts than gabbros. However, the ratios of selected incompatible trace elements with similar partition coefficients (e.g., Nb/La) may be used for basalts and gabbros, because such ratios are less sensitive to fractionation or partial melting processes (Zou and Zindler, 1996; Zou, 2007). Even for gabbro cumulates, these highly incompatible elements are concentrated in the intercumulus liquid. The ratios of these trace element pairs should represent those of the magma from which they crystallized. Thus, some trace element ratios of gabbros are still indicators for contamination/source metasomatism process when treated with caution. Ratios of incompatible elements with similar partition coefficients such as Nb/La and Nb/Th are chosen to constrain the possible crustal contamination/source metasomatism of the gabbros in this study.

All the gabbros are characterized by enrichment of large-ion lithosphere elements (LILE, e.g., Rb, Ba, Sr) and depleted in high-field strength elements (HFSE, e.g., Nb, Ta, Zr, Hf, Ti), with much lower Ta/La ratios (0.01–0.03, except sample ALT039H4) than primitive mantle (i.e., Ta/La = 0.06: Wood et al., 1979). Such distinctive features could be ascribed to involvement of the continental materials because continental crust is typically depleted in Ta and Nb (Barth et al., 2000; Rudnick and Gao, 2003). Crustal components addition might decrease both Nb/La and Nb/Th ratios and result in positive correlation between $\varepsilon_{Nd}(t)$ and Nb/La. However, the analyzed samples show a large range of Nb/La but relatively stable Nb/Th ratios (Fig. 12a) and no correlation between $\varepsilon_{Nd}(t)$ and Nb/La ratios was observed (Fig. 12b). Thus, these features rule out significant crustal contamination. The major and trace elements, whole-rock Sr–Nd and zircon Hf isotopic compositions can be used to decipher their mantle sources and magma evolution process.

6.2. Fractionation/cumulation effects

The gabbros from the Kuwei intrusion and South Kuwei complex shear similar evolutionary trends on bi-variation diagrams, indicating that they followed similar paths of fractionation/accumulation. As shown in thin sections of Kuwei gabbros (Fig. 3d–g), enclosure of olivine in plagioclase and clinopyroxene and reaction rim are observed. Thus, olivine fractionation is significant during the early stage of magma evolution. An increase in CaO, Al_2O_3, CaO/Al_2O_3 with increasing $Mg^{\#}$ supports the fractionation of clinopyroxene (Fig. 8), which is in agreement with the positive correlation of Cr and Ni with $Mg^{\#}$ and (Mg + Fe)/Si rations

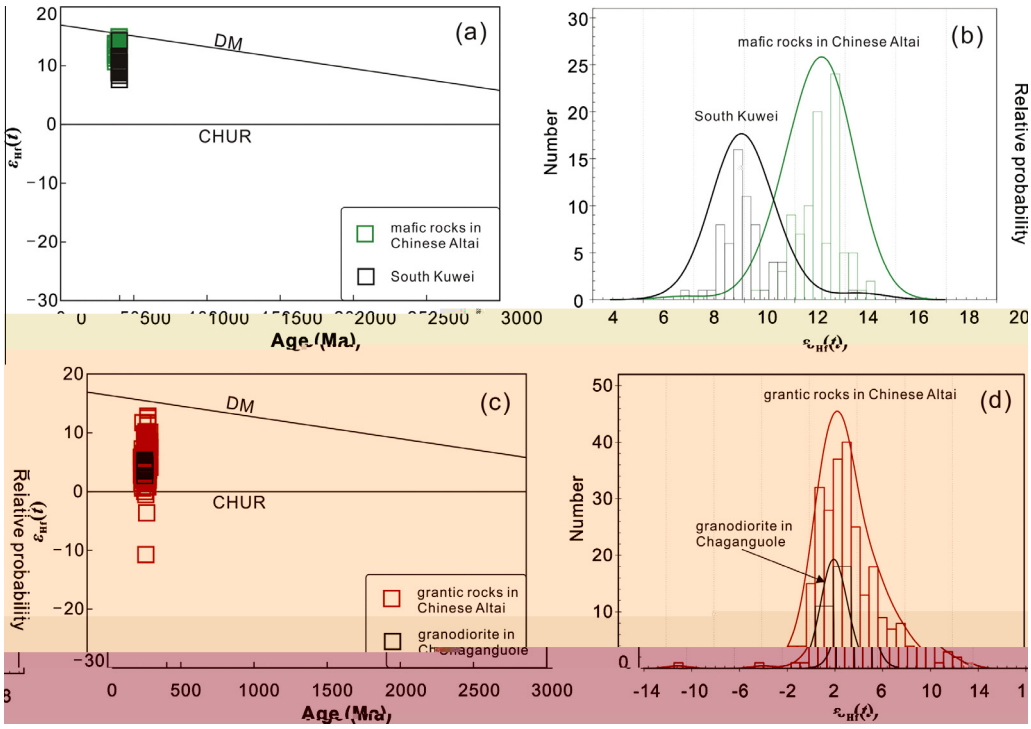

Fig. 11. Histogram of the zircon $\varepsilon_{Hf}(t)$ of mafic rocks and granitoids about ca. 400 Ma along the southern Altai orogen (see detail in text). Data for mafic rocks from Cai et al. (2010), Yao et al. (2013) and granitoids from Cai et al. (2011b, c), Liu et al. (2012), Sun et al. (2008, 2009), Wang et al. (2011).

less than 0.5 (Russell and Nicholls, 1988). A well-defined negative correlation between TiO_2 and $Mg^{\#}$ suggests that Ti was incompatible in the crystallization phases and that titanomagnetite did not reach the solidus. On the incompatible elements spiderdiagrams, the Kuwei complex show positive Sr anomalies and negative P anomalies (Fig. 9b), implying cumulation of plagioclase and fractionation of apatite, which is consistent with their positive Eu anomalies in the REE patterns (Fig. 9a).

As for the gabbros from the South Kuwei complex, the correlation of $Fe_2O_3^T$, CaO and Al_2O_3 with $Mg^{\#}$ is similar to the gabbros from the Kuwei intrusion. The South Kuwai gabbros have (Mg + Fe)/Si ratios less than 0.5, suggesting that clinopyroxene also was an important fractionating mineral in the magma evolution process. Decreasing K_2O and CaO with decreasing of $Mg^{\#}$ in these rocks may reflect fractionation of hornblende, which is consistent with the occurrence of hornblende in these gabbros (Fig. 3). Positive Eu and Sr anomalies and negative P anomalies in multi-element spider diagrams reveal the cumulation of plagioclase and fractionation of apatite (Fig. 9d).

In summary, based on a clear trend between (Mg + Fe)/Ti and Si/Ti (Fig. 13), the magma evolution is mainly governed by fractionation/cumulation of olivine, plagioclase, clinopyroxene coupled with variable fractionation/cumulation of orthopyroxene and hornblende.

6.3. Mantle sources

Close spatial and temporal relationship, similar REE and incompatible elements distribution patterns and positive $\varepsilon_{Nd}(t)$ values (+0.8–+2.2 for the Kuwei intrusion and +3.6–+5.3 for the South Kuwei complex) and positive $\varepsilon_{Hf}(t)$ values (+7.6–+14.3) reveal that these tholeiitic gabbroic rocks were derived from a common time-integrated depleted mantle source. However, the $\varepsilon_{Nd}(t)$ values of these gabbros (including Keketuohai complex from 0 to +2.7) are lower than the coeval basalts from the Kuerti bimodal volcanic sequence (+7.2 to +10.3) that were interpreted to have an asthenospheric origin (Xu et al., 2003; Zhou et al., 2007) (Fig. 10). Furthermore, these rocks show variable LREE-enriched patterns and have

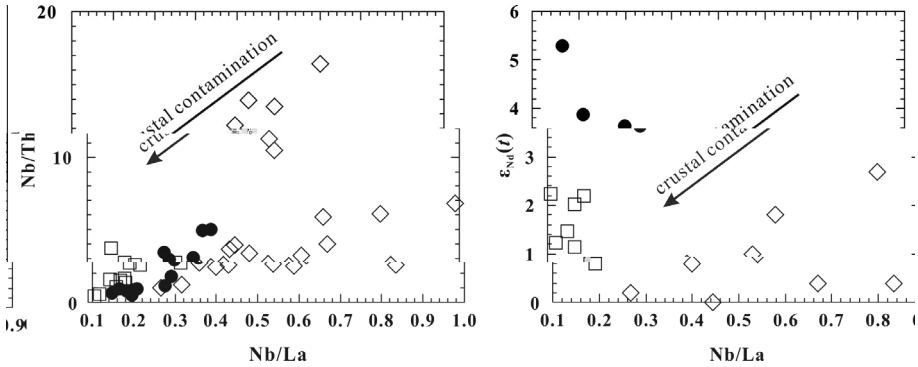

Fig. 12. (a) Nb/Th vs. Nb/La and (b) $\varepsilon Nd(t)$ vs. La/Sm diagrams showing the crustal contamination. Keketuohai data from Cai et al. (2012) (symbols are the same as those in Fig. 7).

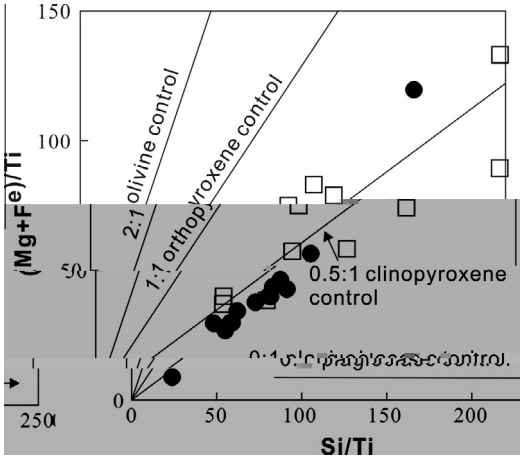

Fig. 13. Pearce elemental ratios diagram showing that the dominant phases is clinopyroxene (symbols are the same as in Fig. 6).

low HFSEs/LREEs ratios (e.g. Nb/La and Ta/La), and these features are uncharacteristic of N-MORB, E-MORB or OIB magmas. Therefore, the primitive magmas of the Kuwei intrusion and South Kuwei complex were most likely derived from lithospheric mantle source.

The enrichment of LILEs and depletion of HFSEs of the Kuwei and South Kuwei complexes may reflect the metasomatism of mantle sources by the influx of slab-released fluids and/or melts derived from partial melting of the subducted slab (Saunders et al., 1991; Stern, 2002; Zhao and Zhou, 2007) because crustal contamination possibility is excluded as mentioned earlier. The studied samples possess high Ba/Nb (37–390), Ba/Zr (2–9), Ba/Th (48–569) and Th/U (1–12) ratios relative to primitive mantle. These elemental ratios are even higher than those of the average upper crust, indicating that they were probably derived from a mantle source modified by hydrous fluids rather than sediment. In $(Hf/Sm)_{PM}$ vs. $(Ta/La)_{PM}$ diagram (Fig. 14a) (Hofmann and Jochum, 1996), all the samples plot into fluid-related subduction metasomatism (except sample ALT039H4). Similarly, the Nb/Zr vs. Th/Zr diagram (Fig. 14b) also reveals that the mantle source was metasomatized by fluids, while for the Keketuohai complex was by both fluids and melts. Base on above analyses, we conclude that the parental magma of the Kuwei intrusion and South Kuwei complex was derive from fluid-metasomatized depleted lithosphere mantle sources. The matasomatism of the mantle sources of the Devonian ultramafic–mafic intrusion belt was most possibly related to Devonian subduction of the Paleo-Asian Oceanic crust. Taking their flat to weak enriched LREE patterns into account, the partial melting of the refractory lithospheric mantle was due to the addition of water liberated from the dehydration of subducting oceanic crust (Fig. 15).

6.4. Implications for the tectonic evolution and continental crust growth

Ultramafic–mafic rocks are usually classified as either Alpine-type or Alaskan-type intrusions in the orogenic belts (Irvine, 1974). The intrusions in this study are characterized by concentric zoning, cumulus textures, occurrence of abundant clinopyroxene and water-bearing minerals such as hornblende and biotite, and the scarcity of orthopyroxene, which resemble the Alaskan-type intrusions. In addition, the diopsidic clinopyroxene has low Ti contents and Al in tetrahedral sites, consistent with those clinopyroxenes from Alaskan-type intrusions (Farahat and Helmy, 2006; Irvine, 1974; Pettigrew and Hattori, 2006). Furthermore, all the hornblendes exhibit negative correlations between Si and Na + K and plot in the typical Alaskan-type complex (Fig. 6b) (Helmy and El Mahallawi, 2003). These features suggest that the Kuwei intrusion and South Kuwei complex are Alaskan-type intrusions.

Alaskan-type ultramafic–mafic complexes are of great significance in the study of orogen evolution (Brügmann et al., 1997; Helmy and El Mahallawi, 2003; Helmy and Mogessie, 2001; Himmelberg and Loney, 1995; Irvine, 1974; Krause et al., 2011; Pertsev and Savelieva, 2005; Su et al., 2012). Previous studies have demonstrated that most Alaskan-type intrusions formed at convergent plate margins, representing arc magmas (Abd El-Rahman et al., 2012; Irvine, 1974; Su et al., 2012, 2013) or arc-root complex (Brügmann et al., 1997; Debari and Coleman, 1989). Both whole-rock elemental geochemistry and rock-forming mineral geochemistry (e.g. clinopyroxene and hornblende) show their typical arc affinities, arguing for their genetic relation to subduction tectonic setting.

In addition, field observations reveal that those Alaskan-type intrusions form a NW-trending belt along the southern margin of the Altai orogen, almost paralleling with the Cambrian to Carboniferous ophiolites belt along the Iritish suture zone or to south of this zone (e.g. Kekesentao ophiolite, Qiaxiahala ophiolite, Qinghe ophiolite, Zhaheba ophiolite, Armantai ophiolite and Kelameili ophiolite) (Fig. 1b), indicating that those complexes are subducting-related. Furthermore, the ca. 400 Ma Chaganguole granodiorite and other granitoids (e.g., Keketuohai granite, Aweitan granite, Kuerti granite, Habahe batholith and Tiereketi batholith) represent the acidic intrusive components and the ca. 400 Ma acidic metavolcanic rocks in Mayinebo Formation and other meta-volcanic rocks (e.g. meta-rhyolites and tuffs in Kangbutiebao Formation)

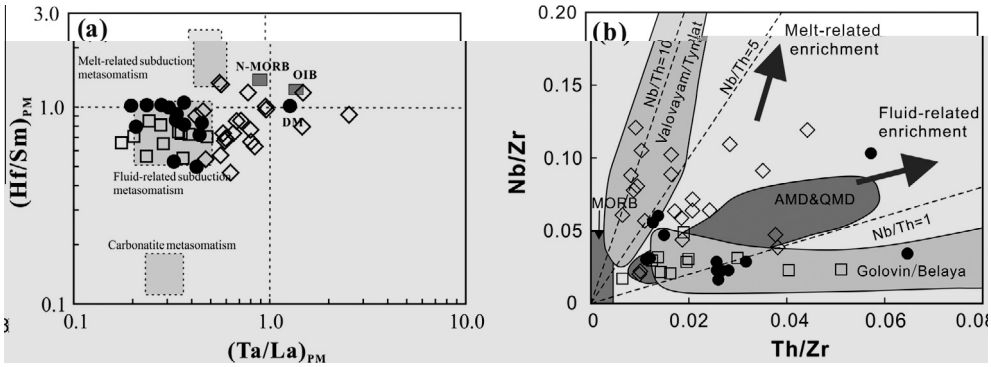

Fig. 14. Plots of (a) $(Hf/Sm)_{PM}$ vs. $(Ta/La)_{PM}$ and (b) Nb/Zr vs. Th/Zr diagrams for gabbros of the Kuwei intrusion and South Kuwei complex. Subscript PM denotes the primitive mantle-normalized. Primitive mantle-normalizing values from Sun and McDonough (1989). Keketuohai data from Cai et al. (2012) (symbols are the same as those in Fig. 7).

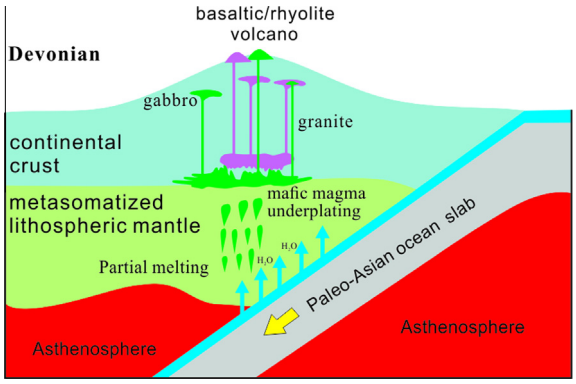

Fig. 15. Cartoon model illustrating the mafic magmas production induced by addition of water liberated from the dehydration of subducting Paleo-Asian Ocean slab and mafic magma underplating at the root of continental arc leading to partial melting of crust.

are eruptive rocks of the Altai arc system. These features indicate that the Devonian tectonic regime of Chinese Altai is linked to Paleo-Asian Ocean subduction.

Apart from Devonian ultramafic–mafic intrusions along the southern Altai orogen, the occurrence of Devonian adakite, boninite (Niu et al., 2006), mafic dykes (Cai et al., 2010) and high temperature metamorphic event (Jiang et al., 2010) may represent a particular tectonic regime. Two major subduction models have been invoked to explain these observations: (1) local collision of continent to continent result in subducting slab break-off (Niu et al., 2006) and (2) ocean ridge subduction (Cai et al., 2010, 2011a, 2011c, 2012; Liu et al., 2012; Jiang et al., 2010; Sun et al., 2009; Windley et al., 2007; Wong et al., 2010).

Granite is the main component of the continental crust on earth. Thus, the growth of the continental crust depends much on the mode of generation of granitoid rocks (Wu et al., 2003). Conventionally, growth of juvenile continental crust is ascribed to occur at subduction zones and mantle plumes. Particularly, the former is the most important for the upper continental crust growth and the later for the lower continental crust (Condie, 1997). The ages of the granitoids along the southern margin of the Altai orogen were dated at 460–375 Ma with a peak at ca. 400 Ma (Sun et al., 2009; Tong et al., 2007, 2006; Wang et al., 2006, 2009; Yuan et al., 2007; Zhang et al., 2006) (Fig. 4f). These granitoids exhibit weak negative to strong positive $\varepsilon_{Nd}(t)$ values (from −2.7 to +3.8) (Chen and Jahn, 2002; Wang et al., 2009; Zhao et al., 1993). In addition, we compiled published Hf isotopic data for granitoids from ca. 400 Ma to ca. 380. Those $\varepsilon_{Hf}(t)$ values show significant positive $\varepsilon_{Hf}(t)$ values (from 0 to +16 with a peak at +5) (Fig. 11c and d), indicating those granitoids were mainly derived from partial melting of juvenile crust.

In the Altai orogen, the close temporal and spatial relationship between granitoids and mafic intrusions argues for their intimate genetic relations. We constructed a cartoon model showing the formation of the Alaskan-type mafic intrusions and the coeval granitoids and volcanic rocks and the possible vertical continental crust growth (Fig. 15).

In this model, during the northward subduction of Paleo-Asian Oceanic crust along the Iritish suture zone, the hydrous fluids released from the subducted slab metasomatized the refractory mantle wedge. Addition of water lowered the solidus and cause metasomatized lithospheric mantle partial melting. The mafic magma derived from metasomatized mantle wedge underplated at the continental arc root, and provided heat to melt the juvenile crust to generate voluminous grantic magmas. In some places, e.g., in Chaganguole region, the fine-grained gabbros intermingled with the granodiorite–granite, possibly due to the mafic magma penetrated the arc and emplaced at a shallow depth with the granitic magmas. Thus, the NW-trending coeval voluminous granites (e.g. Chaganguole granodiorite, Keketuohai granite, Aweitan granite, Kuerti granite, Habahe batholith and Tiereketi batholith) (Cai et al., 2011c; Wang et al., 2006) and the eruptive volcanic rocks (e.g. acidic meta-volcanic rocks in Mayinebo Formation, meta-rhyolites and tuffs in Kangbutiebao Formation) (Chai et al., 2006, 2012a, 2012b and references therein), as well as the ultramafic–mafic complexes, formed an volcanic arc system. In addition, the mafic magmas underplating potentially had significantly contributed to the vertical continental growth of the Altai orogen (Fig. 15).

7. Conclusions

(1) The Kuwei and South Kuwei ultramafic–mafic complexes, as well as the Keketuohai complex and the Habahe gabbroic and doleritic dykes, were generated at 400–380 Ma. Those Devonian ultramafic–mafic intrusions formed a NW-trending Devonian ultramafic–mafic intrusion belt along the southern margin of the Altai orogen.

(2) Textures, mineral compositions, and whole-rock elemental and Nd–Sr–Hf isotope features of the Kuwei and South Kuwei complexes argued that they were cogenetic and formed through fractional crystallization and accumulation of a hydrous, tholeiitic magma. Such magma was derived from a time-integrated depleted lithosphere mantle that was metasomatized by subduction-related fluids. Both their textures and geochemical features display characteristics of typical Alaskan-type complexes.

(3) Arc-like mafic magma underplating at the continental arc root and partial melting of the overlying juvenile crust due to the heating of the mafic magma contributed to the vertical growth of the continental crust in Altai orogen.

Acknowledgements

Mr. Ru-Fu Ding is thanked for his assistance during the field trip. We really appreciate Mr. Guo-Ren Liu for supplying the detailed regional geological map. We are very grateful to Prof. Shuan-Hong Zhang and an anonymous reviewer for their very constructive reviews that significantly improved the quality of this manuscript. This study is financially supported by the Major State Basic Research Program of the PR China (2011CB808903) and the National 305 Project of China (1212011140057).

Appendix A. Supplementary material

Supplementary data associated with this article can be found, in the online version, at http://dx.doi.org/10.1016/j.jseaes.2014.08.008.

References

Abd El-Rahman, Y., Helmy, H.M., Shibata, T., Yoshikawa, M., Arai, S., Tamura, A., 2012. Mineral chemistry of the Neoproterozoic Alaskan-type Akarem Intrusion with special emphasis on amphibole: implications for the pluton origin and evolution of subduction-related magma. Lithos 155, 410–425.

Ao, S.J., Xiao, W.J., Han, C.M., Mao, Q.G., Zhang, J.E., 2010. Geochronology and geochemistry of Early Permian mafic–ultramafic complexes in the Beishan area, Xinjiang, NW China: implications for late Paleozoic tectonic evolution of the southern Altaids. Gondwana Res. 18, 466–478.

Barth, M.G., McDonough, W.F., Rudnick, R.L., 2000. Tracking the budget of Nb and Ta in the continental crust. Chem. Geol. 165, 197–213.

Boynton, W.V., 1984. Geochemistry of the rare earth elements: meteorite studies. In: Henderson, P. (Ed.), Rare Earth Element Geochemistry. Elsevier, pp. 63–114.

Briggs, S.M., Yin, A., Manning, C.E., Chen, Z.L., Wang, X.F., Grove, M., 2007. Late paleozoic tectonic history of the ertix fault in the chinese altai and its

implications for the development of the central Asian orogenic system. Geol. Soc. Am. Bull. 119, 944–960.
Briggs, S.M., Yin, A., Manning, C.E., Chen, Z.L., Wang, X.F., 2009. Tectonic development of the southern Chinese Altai Range as determined by structural geology, thermobarometry, $^{40}Ar/^{39}Ar$ thermochronology, and Th/Pb ion-microprobe monazite geochronology. Geol. Soc. Am. Bull. 121, 1381–1393.
Brügmann, G.E., Reischmann, T., Naldrett, A.J., Sutcliffe, R.H., 1997. Roots of an Archean volcanic arc complex: the Lac des Iles area in Ontario. Canada Precambrian Res. 81, 223–239.
Cai, K.D., Sun, M., Yuan, C., Zhao, G.C., Xiao, W.J., Long, X.P., Wu, F.Y., 2010. Geochronological and geochemical study of mafic dykes from the northwest Chinese Altai: implications for petrogenesis and tectonic evolution. Gondwana Res. 18, 638–652.
Cai, K.D., Sun, M., Yuan, C., Long, X.P., Xiao, W.J., 2011a. Geological framework and Paleozoic tectonic history of the Chinese Altai, NW China: a review. Russ. Geol. Geophys. 52, 1619–1633.
Cai, K.D., Sun, M., Yuan, C., Zhao, G.C., Xiao, W.J., Long, X.P., Wu, F.Y., 2011b. Geochronology, petrogenesis and tectonic significance of peraluminous granites from the Chinese Altai, NW China. Lithos 127, 261–281.
Cai, K.D., Sun, M., Yuan, C., Zhao, G.C., Xiao, W.J., Long, X.P., Wu, F.Y., 2011c. Prolonged magmatism, juvenile nature and tectonic evolution of the Chinese Altai, NW China: evidence from zircon U-Pb and Hf isotopic study of Paleozoic granitoids. J. Asian Earth Sci. 42, 949–968.
Cai, K.D., Sun, M., Yuan, C., Zhao, G.C., Xiao, W.J., Long, X.P., 2012. Keketuohai mafic–ultramafic complex in the Chinese Altai, NW China: petrogenesis and geodynamic significance. Chem. Geol. 294, 26–41.
Chai, F.M., Mao, J.W., Dong, L.H., Yang, F.Q., Liu, F., Geng, X.X., Zhang, Z.X., Huang, C.K., 2006. Geochronology and genesis of the meta-rhyolites in the Kangbutiebao Formation from the Kelang Basin at the southern margin of the Altay, Xinjiang. Acta Petrologica Sinica 25, 1403–1415 (in Chinese with English abstract).
Chai, F.M., Yang, F.Q., Liu, F., Geng, X.X., Zhang, Z.X., Chen, B., 2012a. Geochronology and genesis of the meta-felsic volcanic rocks in the Kangbutiebao Formation from the Maizi Basin at the southern margin of the Altay, Xinjiang. Chinese J. Geol. 47, 221–239 (in Chinese with English abstract).
Chai, F.M., Yang, F.Q., Liu, F., Geng, X.X., Jiang, L.P., Lyu, S.J., Guo, X.J., Chen, B., 2012b. Geochronology and genesis of meta-felsic volcanic rocks from the Kangbutiebao Formation in Chonghuer Basin on southern margin of Altay, Xinjiang. Geol. Rev. 58, 1023–1037 (in Chinese with English abstract).
Chen, B., Jahn, B.M., 2002. Geochemical and isotopic studies of the sedimentary and granitic rocks of the Altai orogen of northwest China and their tectonic implications. Geol. Magzine 139, 1–13.
Chen, B., Jahn, B.M., 2004. Genesis of post-collisional granitoids and basement nature of the Junggar Terrane, NW China: Nd–Sr isotope and trace element evidence. J. Asian Earth Sci. 23, 691–703.
Condie, K.C., 1997. Contrasting sources for upper and lower continental crust: the greenstone connection. J. Geol. 105, 729–736.
Cunningham, D., 2005. Active intracontinental transpressional mountain building in the Mongolian Altai: defining a new class of orogen. Earth Planet. Sci. Lett. 240, 436–444.
Debari, S.M., Coleman, R.G., 1989. Examination of the deep levels of an Island-Arc – evidence from the Tonsina Ultramafic-Mafic Assemblage, Tonsina, Alaska. J. Geophys. Res. Solid 94, 4373–4391.
Farahat, E.S., Helmy, H.M., 2006. Abu Hamamid Neoproterozoic Alaskan-type complex, south Eastern Desert, Egypt. J. Afr. Earth Sci. 45, 187–197.
Geng, J.Z., Li, H.K., Zhang, J., Zhang, Y.Q., 2011. Zircon Hf isotope analysis by means of LA–MC–ICP–MS. Geol. Bull. China 30, 1508–1513 (in Chinese with English abstract).
Han, B.F., 2008. A preliminary comparison of Mesozoic granitoids and rare metal deposits in Chinese and Russian Altai Mountains. Acta Petrologica Sinica 24, 655–660 (in Chinese with English abstract).
Han, B.F., Ji, J.Q., Song, B., Chen, L.H., Zhang, L., 2006. Late Paleozoic vertical growth of continental crust around the Junggar Basin, Xinjiang, China (Part I): timing of post-collisional plutonism. Acta Petrologica Sinica 22, 1077–1086 (in Chinese with English abstract).
Hart, S.R., 1988. Heterogeneous mantle domains: signature, genesis and mixing chronologies. Earth Planet. Sci. Lett. 90, 273–296.
Helmy, H.M., El Mahallawi, M.M., 2003. Gabbro Akarem mafic–ultramafic complex, Eastern Desert, Egypt: a late precambrian analogue of Alaskan-type complexes. Mineral. Petrol. 77, 85–108.
Helmy, H.M., Mogessie, A., 2001. Gabbro Akarem, Eastern Desert, Egypt: Cu–Ni–PGE mineralization in a concentrically zoned mafic–ultramafic complex. Mineral Depositium 36, 58–71.
Himmelberg, G.R., Loney, R.A., 1995. Characteristics and petrogenesis of Alaskan-type ultramafic–mafic intrusions, southeastern Alaska. U.S. Geol. Surv. Prof. Pap., 25–56.
Hofmann, A.W., Jochum, K.P., 1996. Source characteristics derived from very

Su, B.X., Qin, K.Z., Santosh, M., Sun, H., Tang, D.M., 2013. The Early Permian mafic–ultramafic complexes in the Beishan Terrane, NW China: Alaskan-type intrusives or rift cumulates? J. Asian Earth Sci. 66, 175–187.
Sun, S.-S., McDonough, W.F., 1989. Chemical and isotopic systematics of ocean basalts: implications for mantle composition and process. In: Saunders, A.D., Norry, M.J. (Eds.), Magmatism in the Ocean Basins. Geological Society. Special Publications, London, pp. 313–345.
Sun, M., Yuan, C., Xiao, W., Long, X., Xia, X., Zhao, G., Lin, S., Wu, F., Kroner, A., 2008. Zircon U–Pb and Hf isotopic study of gneissic rocks from the Chinese Altai: progressive accretionary history in the early to middle Palaeozoic. Chem. Geol. 247, 352–383.
Sun, M., Long, X.P., Cai, K.D., Jiang, Y.D., Wang, B.Y., Yuan, C., Zhao, G.C., Xiao, W.J., Wu, F.Y., 2009. Early Paleozoic ridge subduction in the Chinese Altai: insight from the abrupt change in zircon Hf isotopic compositions. Sci. China Ser. D – Earth Sci. 52, 1345–1358.
Tong, Y., Wang, T., Kovach, V.P., Hong, D.W., Han, B.F., 2006. Age and origin of the Takeshiken postorogenic alkali-rich intrusive rocks in southern Altai, near the Mongolian border in China and its implications for continental growth. Acta Petrologica Sinica 22, 1267–1278 (in Chinese with English abstract).
Tong, Y., Wang, T., Hong, D.W., Dai, Y.J., Han, B.F., Liu, X.M., 2007. Ages and origin of the early Devonian granites from the north part of Chinese Altai Mountains and its tectonic implications. Acta Petrologica Sinica 23, 1933–1944 (in Chinese with English abstract).
Wan, B., Xiao, W.J., Windley, B.F., Yuan, C., 2013. Permian hornblende gabbros in the Chinese Altai from a subduction-related hydrous parent magma, not from the Tarim mantle plume. Lithosphere 5, 290–299.
Wang, T., Hong, D.W., Jahn, B.M., Tong, Y., Wang, Y.B., Han, B.F., Wang, X.X., 2006. Timing, petrogenesis, and setting of Paleozoic synorogenic intrusions from the Altai Mountains, northwest China: implications for the Tectonic evolution of an accretionary orogen. J. Geol. 114, 735–751.
Wang, T., Jahn, B.-M., Kovach, V.P., Tong, Y., Hong, D.-W., Han, B.-F., 2009. Nd–Sr isotopic mapping of the Chinese Altai and implications for continental growth in the Central Asian Orogenic Belt. Lithos 110, 359–372.
Wang, Y.J., Yuan, C., Long, X.P., Sun, M., Xiao, W.J., Zhao, G.C., Cai, K.D., Jiang, Y.D., 2011. Geochemistry, zircon U–Pb ages and Hf isotopes of the Paleozoic volcanic rocks in the northwestern Chinese Altai: petrogenesis and tectonic implications. J. Asian Earth Sci. 42, 969–985.
White, W.M., Duncan, R.A., 1996. Geochemistry and geochronology of the Society Island: new evidence from deep mantle recycling. In: Basu, A., Hart, S.R. (Eds.), Earth Processes: Reading the Isotopic Code: Geophysical Monograph, vol. 95. AGU, Washington, DC, pp. 183–206.
Windley, B.F., Kroner, A., Guo, J.H., Qu, G.S., Li, Y.Y., Zhang, C., 2002. Neoproterozoic to Paleozoic geology of the Altai orogen, NW China: new zircon age data and tectonic evolution. J. Geol. 110, 719–737.
Windley, B.F., Alexeiev, D., Xiao, W.J., Kroner, A., Badarch, G., 2007. Tectonic models for accretion of the Central Asian Orogenic Belt. J. Geol. Soc., London 164, 31–47.
Wong, K., Sun, M., Zhao, G.C., Yuan, C., Xiao, W.J., 2010. Geochemical and geochronological studies of the Alegedayi Ophiolitic Complex and its implication for the evolution of the Chinese Altai. Gondwana Res. 18, 438–454.
Wood, D.A., Tarneu, J., Varet, J., Saunders, A.N., Bouhault, H., Joron, J.L., Treuil, M., Cann, J.R., 1979. Geochemistry of basalts drills in the North Atlantic by IPOD Leg 49: implications for mantle heterogeneity. Earth Planet. Sci. Lett. 42, 77–97.
Wu, F.Y., Jahn, B.M., Wilde, S.A., Lo, C.H., Yui, T.F., Lin, Q., Ge, W.C., Sun, D.Y., 2003. Highly fractionated I-type granites in NE China (II): isotopic geochemistry and implications for crustal growth in the Phanerozoic. Lithos 67, 191–204.
Wu, F.Y., Yang, Y.H., Xie, L.W., Yang, J.H., Xu, P., 2006. Hf isotopic compositions of the standard zircons and baddeleyites used in U–Pb geochronology. Chem. Geol. 234, 105–126.
implicationPhanerozoic.4(in)-323.4(taleozoic)-2.8(Asian)-328.2(Or..)-321.5eol. 114, Londoemi8.8(164,)30.21612–383